Non-Hermitian Delocalization in a Two-Dimensional Photonic Quasicrystal

Zhaoyang Zhang,[1,*] Shun Liang,[1] Ismaël Septembre,[2] Jiawei Yu,[1] Yongping Huang,[1] Maochang Liu,[3] Yanpeng Zhang,[1] Min Xiao,[4,5] Guillaume Malpuech,[2,†] and Dmitry Solnyshkov[2,6,‡]

[1]*Key Laboratory for Physical Electronics and Devices of the Ministry of Education & Shaanxi Key Lab of Information Photonic Technique, School of Electronic Science and Engineering, Faculty of Electronics and Information, Xi'an Jiaotong University, Xi'an 710049, China*

[2]*Institut Pascal, PHOTON-N2, Université Clermont Auvergne, CNRS, Clermont INP, F-63000 Clermont-Ferrand, France*

[3]*International Research Center for Renewable Energy and State Key Laboratory of Multiphase Flow in Power Engineering, Xi'an Jiaotong University, Xi'an 710049, China*

[4]*Department of Physics, University of Arkansas, Fayetteville, Arkansas 72701, USA*

[5]*National Laboratory of Solid State Microstructures and School of Physics, Nanjing University, Nanjing 210093, China*

[6]*Institut Universitaire de France (IUF), 75231 Paris, France*

(Received 13 February 2024; accepted 28 May 2024; published 27 June 2024)

Theoretical and experimental studies suggest that both Hermitian and non-Hermitian quasicrystals show localization due to the fractal spectrum and to the transition to diffusive bands via exceptional points, respectively. Here, we present an experimental study of a dodecagonal photonic quasicrystal based on electromagnetically induced transparency in a Rb vapor cell. First, we observe the suppression of the wave packet expansion in the Hermitian case. We then discover a new regime, where increasing the non-Hermiticity leads to delocalization, demonstrating that the behavior in non-Hermitian quasicrystals is richer than previously thought.

DOI: 10.1103/PhysRevLett.132.263801

Quasicrystals are characterized by long-range order without translational symmetry [1]. In mathematics, they correspond to infinite nonperiodic tilings. They can possess rotational symmetries incompatible with the translational one, such as the famous pentagonal symmetry of the Penrose tiling [2]. Another interesting and important case is the dodecagonal symmetry [3–5], which can be obtained from a superposition of two honeycomb lattices [6–9] rotated by 30°. This configuration is particularly timely because of the extreme popularity of moiré honeycomb lattices such as magic-angle twisted bilayer graphene [10], obtained for angles of rotation smaller than 30°. Moiré lattices and quasicrystals share many common properties, such as the presence of flat bands [11–13] in their spectrum. Dodecagonal quasicrystals are studied in many fields: chemistry [14–17], material science [4,18,19], electronics [8], topological physics [20–22], and photonics [7,23–31].

For 1D quasicrystals or quasiperiodic lattices, many important analytical results were obtained using the Aubry-André model [32]: instead of considering a structure without translational symmetry in the positions of individual sites, one considers a periodic lattice with an incommensurate on-site potential of a variable strength [33–36]. It is now theoretically established and experimentally demonstrated that the dispersion of such a 1D quasicrystal contains an infinite number of gaps that obey the gap labeling theorem [37–40]. Each single band is infinitely narrow (flat), and the mobility of the particles filling the bands is strongly suppressed [33,41]. This model allows studying the transition toward the fractal energy spectrum and the associated localization [42], driven by the variable strength of the on-site potential.

Two-dimensional quasicrystals have also been studied theoretically using the Aubry-André approach [13], namely considering a superposition of two lattices: one lattice is fixed, while the strength of the second lattice is varied, allowing to observe the modification of the transport. Another theoretical approach was to start directly with a quasicrystal potential and vary its strength relative to the recoil energy [43–46], allowing to see the localization of some of the eigenstates described by their inverse participation ratio. The bands tend to a Cantor set analog [47], as in 1D [48]. In experiments with Hermitian 2D quasicrystals, phononic [49] and photonic [50] band gaps were explicitly observed, in particular in dodecagonal structures [25]. Localization in photonic quasicrystals of different symmetries has been demonstrated very recently [51], and also the enhancement of the transport by disorder [52].

The potential can also be imaginary, making possible non-Hermitian phenomena analogous to the PT-symmetry-breaking transition, well-known in modern photonics [53]. Such transition has recently been predicted [36] and observed experimentally [54] in a 1D quasicrystal: increasing the non-Hermiticity induces a phase transition, which ultimately suppresses the mobility edge. All states become localized, and the mechanism is not due anymore to the

quasicrystal flat bands, but to the emergence of diffusive non-Hermitian bands (Fermi arcs limited by exceptional points). The Aubry-André approach has often been used for non-Hermitian systems [55–57]. Theoretical analyses of 2D systems have also been performed, based on a specific complex potential case [58], as the one considered in the 1980s [59], with results similar to 1D.

In this Letter, we take advantage of a reconfigurable photonic platform, atomic vapors under electromagnetically induced transparency (EIT) [60] in a three-level atomic configuration [61–63], to perform an experimental study of a 2D Hermitian and non-Hermitian dodecagonal quasicrystals with a tunable ratio of intensities between the two honeycomb lattices forming the quasicrystal and a separately controllable non-Hermiticity. We demonstrate the localization transition with the increase of the intensity ratio of two lattices in the Hermitian case. On the contrary, in the non-Hermitian case the initial localization is followed by a delocalization. The latter is caused by the wave packet redistribution due to the lifetime difference, occurring without crossing exceptional points.

The experimental scheme is shown in Fig. 1(a). Two honeycomb photonic lattices are optically induced inside a Rb vapor cell by two hexagonal coupling beams $\boldsymbol{E}_{c1}$ (frequency ω_{c1}) and $\boldsymbol{E}_{c2}$ (ω_{c2}) with the same period of 200 μm, injected into the vapor cell along the z direction [Fig. 1(a) is just a sketch, the experimental lattices are much larger]. There exists a rotation angle (in the x–y plane) of 30° between the two hexagonal patterns. A weak Gaussian probe beam $\boldsymbol{E}_p$ (ω_p) from a continuous-wave tunable laser copropagates with the coupling beams to excite a three-level atomic configuration (Fig. S1 in Supplemental Material [64]), where the well-known EIT effect can occur at appropriate detunings satisfying the two-photon resonance [60] $\delta_p - \delta_{c1}(\delta_{c2}) = 0$. The frequency detunings δ_i ($i = p$, $c1$, and $c2$) are defined as the difference between the frequency of laser field $\boldsymbol{E}_i$ and the levels it connects (see Ref. [64]). Under the EIT condition, the susceptibility χ experienced by $\boldsymbol{E}_p$ is inversely related to the intensity of the coupling beams [65,66]. The superposition intensity of two coupling beams is shown in Fig. 1(b). Each coupling beam forms a single honeycomb photonic lattice (dark sites of the hexagonal pattern). The propagation of a probe beam through the vapor cell with an EIT-induced susceptibility distribution is described by the paraxial equation

$$i\frac{\partial E}{\partial z} = -\frac{1}{2k_0}\Delta E - \frac{k_0\chi}{2}E, \tag{1}$$

where k_0 is the probe wave vector. This is equivalent to a 2D time-dependent Schrödinger equation with $z \sim t$ (time), $k_0 \sim m$ (particle mass), and $\chi \sim -U$ (external potential). Susceptibility maxima [dark sites in Fig. 1(b)] thus correspond to potential minima.

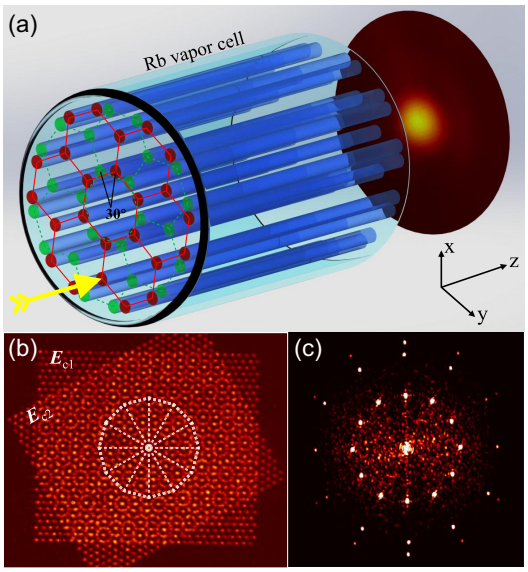

FIG. 1. (a) Experimental scheme. (b) The experimentally generated dodecagonal quasicrystal lattice formed by two hexagonal patterns rotated by 30°. (c) Reciprocal-space image of the experimental quasicrystal lattice exhibiting a twelvefold symmetry in 3 orders of diffraction.

The transmitted probe beam is received by a charge-coupled device camera (placed behind the output plane of the cell) through an imaging lens. During the experiment, the detuning of the probe beam is set as $\delta_p = -260$ MHz, while δ_{c1} and δ_{c2} are manipulated [around positive two-photon detuning $\delta_p - \delta_{c1}(\delta_{c2})$] to control the degree of non-Hermiticity of the induced photonic lattice (detunings are in [64]). The twelvefold symmetry of the resulting lattice is underlined in Fig. 1(b) by the white dodecagon. Figure 1(c) shows the reciprocal-space image also exhibiting a twelvefold pattern with the first three diffraction orders clearly visible, which confirms the formation of a quasicrystal [8].

We study the evolution of the probe beam in the quasicrystal potential created by the coupling beams (under the limitations of the experimental method, see section I.C in [64]). The probe beam represents a narrow wave packet (comparable to a single lattice site), its approximate injection point is shown by a yellow arrow in Fig. 1(a). The duration of the time evolution in the 2D Schrödinger equation is fixed by the length of the vapor cell in the z direction. It is sufficient for the wave packet to expand over several unit cells in a honeycomb lattice (its maximum is not necessarily at the injection point), whereas in the quasicrystal configuration the expansion is expected to be suppressed.

Figure 2 presents the results obtained in the fully Hermitian case. We keep one honeycomb lattice turned on with a constant intensity I_1, while varying the intensity I_2 of the second lattice. The top panels Figs. 2(a)–2(c) show

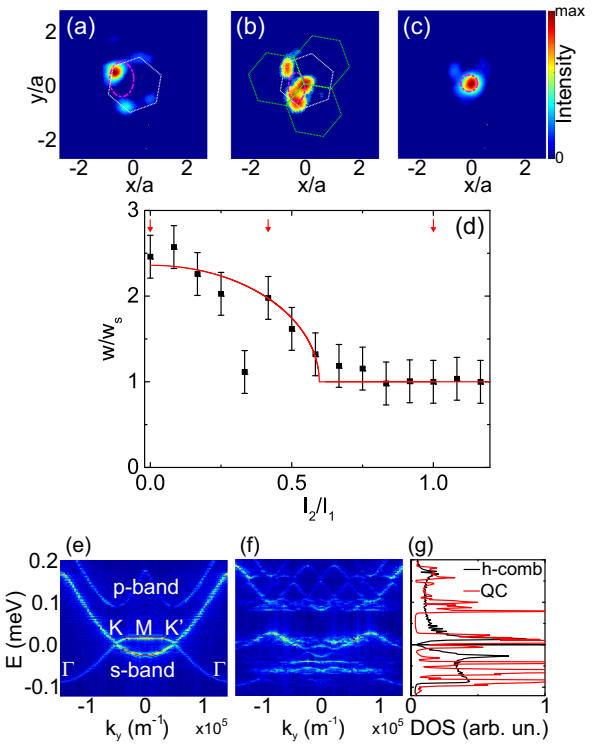

FIG. 2. Wave packet expansion and the localization transition with the increase of the second lattice strength. (a)–(c) Spatial images of the wave packet after its evolution in the Hermitian lattice (lattice intensity ratio $I_2/I_1 = 0, 0.4, 1$, respectively), magenta line marks the wave packet size. (d) Wave packet width w normalized by the lattice site width w_s. Red arrows mark the correspondence with panels (a)–(c). (e) The dispersion of a single honeycomb lattice through $\Gamma KMK'\Gamma'$ points. (f) The dispersion of a quasicrystal showing multiple gaps. (g) The comparison of the DOS for a periodic honeycomb lattice and a quasicrystal. The gaps appear as zeroes of the DOS.

the spatial distribution of the output probe patterns for three ratios of I_2/I_1 (0, 0.4, 1, respectively). The cells of the two lattices are indicated in Figs. 2(a) and 2(b) with white and green dashed hexagons. Magenta dashed ellipses indicate the wave packet width defined as the standard deviation, which is a square root of the second moment of the distribution (the variance). A clear narrowing of the output wave packet can be observed. We note that it is perfectly normal that the standard deviation of a multimodal distribution with different peak heights is smaller than the distance between these peaks [64,67]. We have systematically studied the width of the output wave packet as a function of the ratio I_2/I_1. The results are shown in Fig. 2(d) with black dots with error bars corresponding to the uncertainty of the extraction. For a full set of images see Ref. [64] or an online movie [68].

The output width of the wave packet exhibits a continuous decrease (apart from a special localization point [69]) until it drops to its minimal size, approximately corresponding to the size of a single lattice site w_s that we take as a reference for this plot. To explain this behavior and to determine the transition point, we have performed numerical simulations based on Eq. (1) (see Ref. [64] for details). An example of the dispersion of a single honeycomb lattice is shown in Fig. 2(e). It is plotted along the $\Gamma KMK'\Gamma$ high-symmetry points. As expected [47,48], the increase of I_2/I_1 up to 1 opens a set of gaps in the dispersion, making the band similar to a Cantor set. An example of the dispersion for $I_2/I_1 = 1$ is shown in Fig. 2(f). It exhibits a lot of gaps separating narrowing bands. The density of states (DOS) allows us to detect and analyze full gaps. Figure 2(g) shows the DOS for the two cases shown in panels (e) and (f): honeycomb lattice and dodecagonal quasicrystal. The Dirac point is visible for the honeycomb lattice (black) as a zero-DOS point with linear behavior in its vicinity. In the quasicrystal case (red), multiple large gaps accompanied by narrower secondary gaps are visible. The edges of each gap demonstrate Van Hove singularities (DOS peaks).

The wave packet expansion is determined by the group velocity of its components. If the wave packet is narrow in real space, it covers the whole Brillouin zone and thus allows probing the *maximal* group velocity available. Our simulations show that the first (and largest) gap is opened precisely at the point of highest group velocity, because here the wave function is the most sensitive to the perturbing potential. It corresponds to the ΓK direction, where the dispersion of a single honeycomb lattice is given by $E(k) = \pm J(1 + 2\cos ka/2)$ in the tight-binding limit, and the group velocity is $v_g(k) = \pm\hbar^{-1}Ja\sin ka/2$, with the maximal v_g point $k_{\max} = \pi/a$. The gap size Δ is linearly proportional to the strength of the incommensurate potential $\lambda = I_2/I_1$ for small perturbations: $\Delta \sim \lambda$. This allows estimating the wave packet expansion via the group velocity [64] as a function of the perturbation strength λ,

$$\frac{w(I_2/I_1)}{w_s} = 1 + A\sqrt{1 - B\left(\frac{I_2}{I_1}\right)^2}, \tag{2}$$

where A links the group velocity and the wave packet width (including the effective propagation time), while B links the gap size Δ and the perturbation λ. The red curve in Fig. 2(d) fits the experimental data with Eq. (2), giving the fitting parameters $A \approx 1.35 \pm 0.09$ and $B \approx 2.81 \pm 0.12$. The value of A is directly determined by the wave packet size at $I_2 = 0$ in Fig. 2(d). The value of B allows determining the localization transition point $(I_2/I_1)_{\text{loc}} = \sqrt{1/B} \approx 0.597 \pm 0.013$, of the same order of magnitude as in other quasicrystals [13]. We conclude that we have observed a localization transition for a Hermitian 2D dodecagonal quasicrystal and found its approximate position. The transition point depends on the particular periodic potential.

We now turn to the non-Hermitian case by changing the probe detuning. Indeed, the EIT configuration allows

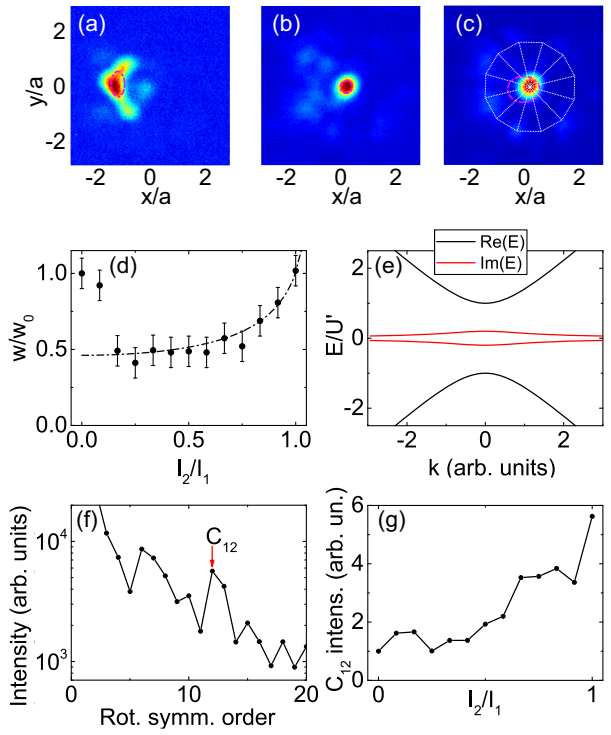

FIG. 3. Localization-delocalization transition in a 2D non-Hermitian quasicrystal. (a)–(c) Spatial images of the wave packet after its evolution in the non-Hermitian lattice (lattice intensity ratio $I_2/I_1 = 0.1, 0.4, 1$, respectively). Magenta line marks the wave packet size. (d) Wave packet width w normalized by the reference width w_0 (corresponding to $I_2/I_1 = 0$). Points with error bars (instrumental uncertainty)—experiment, dash-dotted line—theory. (e) Real (black) and imaginary (red) parts of the eigenenergies of the weak complex potential model. (f) Fourier transform of the angular pattern of the panel (c) ($I_2/I_1 = 1$) exhibiting a maximum corresponding to dodecagonal symmetry C_{12}. (g) Intensity of the C_{12} maximum of the Fourier transform as a function of I_2/I_1: the symmetry of the wave packet inherits that of the lattice.

varying both real and imaginary parts of the effective potential via the complex susceptibility, potentially providing an important non-Hermiticity to the potential. It ultimately allows observing a transition similar to the PT-symmetry-breaking one [63], but we remain below this transition, defined by $(\chi''/\chi')_{\text{crit}} \approx 0.4$. Here, $(\chi''/\chi') \approx 0.2$. We fix the intensity I_1 of the first honeycomb lattice and vary the other intensity I_2, with both lattices being non-Hermitian. We note that the real part of the potential is different from that of Figs. 2(a)–2(d).

Figures 3(a)–3(c) shows the spatial images of the output beam for three values of I_2/I_1 (0.1, 0.4, and 1, respectively). Interestingly, after the onset of localization, the wave packet expansion is recovered almost completely, and the symmetry of the final wave packet changes. Figure 3(d) shows the wave packet size w (black dots) normalized by the size w_0 observed for a single honeycomb lattice $I_2/I_1 = 0$ (for a full set of images see Ref. [64] or an online movie). The measurements demonstrate first a rapid decrease and then an increase of the width, with a minimum around $I_2/I_1 \approx 0.4$.

To understand this behavior, we use the weak potential approximation and work with an effective Hamiltonian (see Ref. [64]). This allows us to obtain the asymptote shown in Fig. 3(d) with a black dash-dotted line. It describes the wave packet broadening due to the non-Hermitian mechanism described by the following Hamiltonian:

$$H = \alpha(k - k_0)\sigma_z + U'\sigma_x + iU''\sigma_x. \tag{3}$$

This Hamiltonian exhibits exceptional points if $U' = 0$, that is, if the potential is purely imaginary. The position of exceptional points is determined by $(k^* - k_0) = \pm U''/\alpha$. In our case, they are not accessible, since $U' \neq 0$. Nevertheless, the non-Hermitian nature of the Hamiltonian leads to important consequences: the decay rate of the states starts to depend on their wave vector. The eigenvalues are given by $E(k - k_0) = \pm\sqrt{U'^2(1 - i\lambda)^2 + \alpha^2(k - k_0)^2}$. Figure 3(e) shows the corresponding correction to the overall decay rate. The resulting decay rate profile leads to the concentration of the wave packet at longest-living states in the reciprocal space at the edge of the largest gap. Because of this, the wave packet width in real space grows as a function of the ratio of the two lattices for fixed evolution time t, according to the following law [64]:

$$\Delta r = \frac{C}{\sqrt{1 - D(\frac{I_2}{I_1})^2}}. \tag{4}$$

Figure 3(d) shows a fitting with $C \approx 0.46 \pm 0.02$ (consistent with Fig. 2, the wave packet expansion gives a factor $C^{-1} \approx 2$ with respect to a single site) and $D \approx 0.79 \pm 0.02$ (meaning that the characteristic decay length due to the non-Hermiticity is shorter than the vapor cell length [64], in agreement with the experiment). The theoretical curve presents a good agreement with the experimental data. We therefore conclude that while in periodic systems the non-Hermiticity can lead to localization via the PT-symmetry-breaking transition, in our quasicrystal we observe that the non-Hermiticity leads to delocalization in wave packet expansion. We note that delocalization has been observed in pentagonal quasicrystals [52], but there it was induced by disorder and not by non-Hermiticity.

Contrary to the Hermitian case, where the wave packet localization width is comparable to the size of a single lattice site w_s, the non-Hermitian case, thanks to the suppression of the localization, allows observing the wave packet distribution over several neighboring sites for $I_2/I_1 = 1$ (exact quasicrystal limit). We analyze the angular distribution of this wave packet (the probability density averaged over the radial coordinate r) by performing its Fourier transform [Fig. 3(f)]. A clear maximum corresponding to the dodecagonal (C_{12}) symmetry is observed.

The corresponding dodecagon is marked in Fig. 3(c) with white dashed lines. This confirms that the wave packet inherits the symmetry of the quasicrystal lattice. We also study the behavior of the C_{12} maximum of the angular Fourier transform with the intensity of the second lattice I_2/I_1 in Fig. 3(g) (normalized to its "background" value at $I_2/I_1 = 0$) and observe a strong growth of this component above $I_2/I_1 \approx 0.6$, when the wave packet delocalization takes place. This confirms that for small intensity of the second lattice its effect can be seen as an incommensurate (effectively random) on-site potential for the initial (honeycomb) lattice, whereas for large intensities the superposition of two lattices must be indeed considered as a dodecagonal quasicrystal with associated properties.

To conclude, we have studied the beam evolution in a reconfigurable photonic platform, allowing us to continuously analyze the transition between a crystal and a quasicrystal both in Hermitian and non-Hermitian cases. We have observed an efficient localization of the beam in Hermitian quasicrystals. We have also shown that the combination of two localizing contributions (incommensurate potential and non-Hermiticity) can actually lead to delocalization, allowing us to recover almost the same transport properties as for a single periodic honeycomb Hermitian lattice, but with the wave packet symmetry becoming dodecagonal. A similar non-Hermitian delocalization effect could also take place in moiré lattices. Our results can find direct applications for on-demand beam tailoring [70–72]. Generally speaking, the applications of quasicrystals in photonics go beyond the localization [50], waveguiding [73], and beam focusing [74]: in particular, they were also shown to exhibit negative refraction [26].

This work was supported by National Natural Science Foundation of China (No. 52488201, No. 62022066, and No. 12074306) and European Union's Horizon 2020 program, through a FET Open research and innovation action under the Grant agreement No. 964770 (TopoLight). We also acknowledge the support of the ANR Labex Ganex (ANR-11-LABX-0014), the ANR projects NEWAVE and MoirePlusPlus, and of the ANR program "Investissements d'Avenir" through the IDEX-ISITE initiative 16-IDEX-0001 (CAP 20-25).

*Corresponding author: zhyzhang@xjtu.edu.cn
†Corresponding author: guillaume.malpuech@uca.fr
‡Corresponding author: dmitry.solnyshkov@uca.fr

[1] D. Levine and P. J. Steinhardt, Phys. Rev. Lett. **53**, 2477 (1984).
[2] D. Shechtman, I. Blech, D. Gratias, and J. W. Cahn, Phys. Rev. Lett. **53**, 1951 (1984).
[3] T. Ishimasa, H.-U. Nissen, and Y. Fukano, Phys. Rev. Lett. **55**, 511 (1985).
[4] Q. B. Yang and W. D. Wei, Phys. Rev. Lett. **58**, 1020 (1987).
[5] F. Gahler, in *Quasicrystalline Materials: Proceedings of the I.L.L. / Codest Workshop, Grenoble, 1988*, edited by C. Janot (World Scientific, Singapore, 1988), chap. 7, pp. 272–284.
[6] N. Niizeki and H. Mitani, J. Phys. A **20**, L405 (1987).
[7] X. Zhang, Z.-Q. Zhang, and C. T. Chan, Phys. Rev. B **63**, 081105(R) (2001).
[8] S. J. Ahn, P. Moon, T.-H. Kim, H.-W. Kim, H.-C. Shin, E. H. Kim, H. W. Cha, S.-J. Kahng, P. Kim, M. Koshino *et al.*, Science **361**, 782 (2018).
[9] J. Crosse and P. Moon, Sci. Rep. **11**, 11548 (2021).
[10] E. Y. Andrei and A. H. MacDonald, Nat. Mater. **19**, 1265 (2020).
[11] G. Tarnopolsky, A. J. Kruchkov, and A. Vishwanath, Phys. Rev. Lett. **122**, 106405 (2019).
[12] P. Moon, M. Koshino, and Y.-W. Son, Phys. Rev. B **99**, 165430 (2019).
[13] B. Huang and W. V. Liu, Phys. Rev. B **100**, 144202 (2019).
[14] K. Hayashida, T. Dotera, A. Takano, and Y. Matsushita, Phys. Rev. Lett. **98**, 195502 (2007).
[15] J. Zhang and F. S. Bates, J. Am. Chem. Soc. **134**, 7636 (2012).
[16] T. M. Gillard, S. Lee, and F. S. Bates, Proc. Natl. Acad. Sci. U.S.A. **113**, 5167 (2016).
[17] A. Jayaraman, C. M. Baez-Cotto, T. J. Mann, and M. K. Mahanthappa, Proc. Natl. Acad. Sci. U.S.A. **118**, e2101598118 (2021).
[18] S. Fischer, A. Exner, K. Zielske, J. Perlich, S. Deloudi, W. Steurer, P. Lindner, and S. Förster, Proc. Natl. Acad. Sci. U.S.A. **108**, 1810 (2011).
[19] C. Xiao, N. Fujita, K. Miyasaka, Y. Sakamoto, and O. Terasaki, Nature (London) **487**, 349 (2012).
[20] Y. E. Kraus, Z. Ringel, and O. Zilberberg, Phys. Rev. Lett. **111**, 226401 (2013).
[21] D.-T. Tran, A. Dauphin, N. Goldman, and P. Gaspard, Phys. Rev. B **91**, 085125 (2015).
[22] C.-B. Hua, R. Chen, B. Zhou, and D.-H. Xu, Phys. Rev. B **102**, 241102(R) (2020).
[23] Y. S. Chan, C. T. Chan, and Z. Y. Liu, Phys. Rev. Lett. **80**, 956 (1998).
[24] M. Kaliteevski, S. Brand, R. Abram, T. Krauss, R. D. Rue, and P. Millar, Nanotechnology **11**, 274 (2000).
[25] M. Zoorob, M. Charlton, G. Parker, J. Baumberg, and M. Netti, Nature (London) **404**, 740 (2000).
[26] Z. Feng, X. Zhang, Y. Wang, Z.-Y. Li, B. Cheng, and D.-Z. Zhang, Phys. Rev. Lett. **94**, 247402 (2005).
[27] W. Man, M. Megens, P. J. Steinhardt, and P. M. Chaikin, Nature (London) **436**, 993 (2005).
[28] R. C. Gauthier and K. Mnaymneh, Opt. Express **13**, 1985 (2005).
[29] K. Nozaki and T. Baba, Jpn. J. Appl. Phys. **45**, 6087 (2006).
[30] J. Ren, X. Sun, and S. Wang, Opt. Laser Technol. **101**, 42 (2018).
[31] X. Xi and X. Sun, Superlattices Microstruct. **129**, 247 (2019).
[32] S. Aubry and G. André, Ann. Isr. Phys. Soc. **3**, 133 (1980).
[33] Y. Lahini, R. Pugatch, F. Pozzi, M. Sorel, R. Morandotti, N. Davidson, and Y. Silberberg, Phys. Rev. Lett. **103**, 013901 (2009).

[34] S. Ganeshan, K. Sun, and S. Das Sarma, Phys. Rev. Lett. **110**, 180403 (2013).
[35] G. Domínguez-Castro and R. Paredes, Eur. J. Phys. **40**, 045403 (2019).
[36] S. Longhi, Phys. Rev. Lett. **122**, 237601 (2019).
[37] B. Simon, Adv. Appl. Math. **3**, 463 (1982).
[38] J. Bellissard, A. Bovier, and J.-M. Ghez, Rev. Math. Phys. **4**, 1 (1992).
[39] J.-M. Gambaudo and P. Vignolo, New J. Phys. **16**, 043013 (2014).
[40] D. Tanese, E. Gurevich, F. Baboux, T. Jacqmin, A. Lemaître, E. Galopin, I. Sagnes, A. Amo, J. Bloch, and E. Akkermans, Phys. Rev. Lett. **112**, 146404 (2014).
[41] G. Roati, C. D'Errico, L. Fallani, M. Fattori, C. Fort, M. Zaccanti, G. Modugno, M. Modugno, and M. Inguscio, Nature (London) **453**, 895 (2008).
[42] V. Goblot, A. Štrkalj, N. Pernet, J. L. Lado, C. Dorow, A. Lemaître, L. Le Gratiet, A. Harouri, I. Sagnes, S. Ravets *et al.*, Nat. Phys. **16**, 832 (2020).
[43] K. Ueda and H. Tsunetsugu, Phys. Rev. Lett. **58**, 1272 (1987).
[44] A. Szabó and U. Schneider, Phys. Rev. B **101**, 014205 (2020).
[45] R. Gautier, H. Yao, and L. Sanchez-Palencia, Phys. Rev. Lett. **126**, 110401 (2021).
[46] Z. Zhu, S. Yu, D. Johnstone, and L. Sanchez-Palencia, Phys. Rev. A **109**, 013314 (2024).
[47] D. Damanik and A. Gorodetski, Commun. Math. Phys. **305**, 221 (2011).
[48] A. Sütő, J. Stat. Phys. **56**, 525 (1989).
[49] S. He and J. D. Maynard, Phys. Rev. Lett. **62**, 1888 (1989).
[50] Z. V. Vardeny, A. Nahata, and A. Agrawal, Nat. Photonics **7**, 177 (2013).
[51] P. Wang, Q. Fu, V. V. Konotop, Y. V. Kartashov, and F. Ye, Nat. Photonics **224**, 18 (2024).
[52] L. Levi, M. Rechtsman, B. Freedman, T. Schwartz, O. Manela, and M. Segev, Science **332**, 1541 (2011).
[53] Ş. Özdemir, S. Rotter, F. Nori, and L. Yang, Nat. Mater. **18**, 783 (2019).
[54] Q. Lin, T. Li, L. Xiao, K. Wang, W. Yi, and P. Xue, Phys. Rev. Lett. **129**, 113601 (2022).
[55] Q.-B. Zeng, Y.-B. Yang, and Y. Xu, Phys. Rev. B **101**, 020201(R) (2020).
[56] T. Li, Y.-S. Zhang, and W. Yi, Phys. Rev. B **105**, 125111 (2022).
[57] A. Padhan, S. R. Padhi, and T. Mishra, Phys. Rev. B **109**, L020203 (2024).
[58] Z.-H. Xu, X. Xia, and S. Chen, Sci. China **65**, 227211 (2022).
[59] P. Sarnak, Commun. Math. Phys. **84**, 377 (1982).
[60] J. Gea-Banacloche, Y.-q. Li, S.-z. Jin, and M. Xiao, Phys. Rev. A **51**, 576 (1995).
[61] Z. Zhang, F. Li, G. Malpuech, Y. Zhang, O. Bleu, S. Koniakhin, C. Li, Y. Zhang, M. Xiao, and D. D. Solnyshkov, Phys. Rev. Lett. **122**, 233905 (2019).
[62] Z. Zhang, S. Liang, F. Li, S. Ning, Y. Li, G. Malpuech, Y. Zhang, M. Xiao, and D. Solnyshkov, Optica **7**, 455 (2020).
[63] Z. Zhang, Y. Feng, S. Ning, G. Malpuech, D. Solnyshkov, Z. Xu, Y. Zhang, and M. Xiao, Photonics Res. **10**, 958 (2022).
[64] See Supplemental Material at http://link.aps.org/supplemental/10.1103/PhysRevLett.132.263801 for extra experimental data and more details on the experiment and on the theory.
[65] Z. Zhang, R. Wang, Y. Zhang, Y. V. Kartashov, F. Li, H. Zhong, H. Guan, K. Gao, F. Li, Y. Zhang *et al.*, Nat. Commun. **11**, 1902 (2020).
[66] Y. Feng, Z. Liu, F. Liu, J. Yu, S. Liang, F. Li, Y. Zhang, M. Xiao, and Z. Zhang, Phys. Rev. Lett. **131**, 013802 (2023).
[67] B. S. Everitt and D. J. Hand, *Finite Mixture Distributions* (Chapman and Hall, London, 1981).
[68] https://www.youtube.com/watch?v=xERIOxb7muE
[69] The special localization point visible in Fig. 2(d) for $I_2/I_0 \approx 0.3$ occurs because some localized states appear in a perturbed periodic potential even before the fractalization of the energy spectrum. If the probe has a strong overlap with such state, the wave packet will not expand, even though there are still propagative states available in some bands: they are simply not excited efficiently. The recovery of the expansion with the increase of the second lattice potential I_2 confirms the occasional nature of this localization. On the contrary, the expansion is definitively suppressed once the true localization threshold is passed.
[70] E. Miyai, K. Sakai, T. Okano, W. Kunishi, D. Ohnishi, and S. Noda, Nature (London) **441**, 946 (2006).
[71] B. Perez-Garcia, C. López-Mariscal, R. I. Hernandez-Aranda, and J. C. Gutiérrez-Vega, Appl. Opt. **56**, 6967 (2017).
[72] Q. Fu, P. Wang, C. Huang, Y. V. Kartashov, L. Torner, V. V. Konotop, and F. Ye, Nat. Photonics **14**, 663 (2020).
[73] C. Jin, B. Cheng, B. Man, Z. Li, D. Zhang, S. Ban, and B. Sun, Appl. Phys. Lett. **75**, 1848 (1999).
[74] E. Di Gennaro, D. Morello, C. Miletto, S. Savo, A. Andreone, G. Castaldi, V. Galdi, and V. Pierro, Photonics Nanostruct. Fundam. Appl. **6**, 60 (2008).